Non-injection Synthesis of Doped Zinc Oxide Plasmonic Nanocrystals

Enrico Della Gaspera,* Anthony S. R. Chesman, Joel van Embden, and Jacek J. Jasieniak*

CSIRO Manufacturing Flagship, Bayview Avenue, Clayton, Victoria 3168, Australia

ABSTRACT Plasmonic metal oxide nanocrystals bridge the optoelectronic gap between semiconductors and metals. In this study, we report a facile, non-injection synthesis of ZnO nanocrystals doped with Al, Ga, or In. The reaction readily permits dopant/zinc atomic ratios of over 15%, is amenable to high precursor concentrations (0.2 M and greater), and provides high reaction yields (>90%). The resulting colloidal dispersions exhibit high transparency in the visible spectrum and a wavelength-tunable infrared absorption, which arises from a dopant-induced surface plasmon resonance. Through a detailed investigation of reaction parameters, the reaction mechanism is fully characterized and correlated to the optical properties of the synthesized nanocrystals. The distinctive optical features of these doped nanocrystals are shown to be readily harnessed within thin films that are suitable for optoelectronic applications.

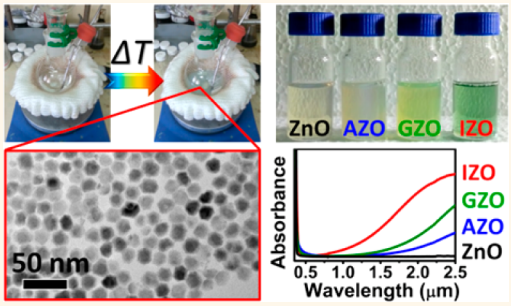

KEYWORDS: ZnO · nanoparticles · surface plasmon resonance · doping · colloidal synthesis · optical properties

Nonmetallic plasmonic nanocrystals (NCs) are rapidly emerging as new materials for optoelectronics, photocatalysis, and electrochemistry.[1−11] In particular, n-type-doped metal oxides have recently gained interest due to their remarkable optical and electrical properties with respect to their undoped counterparts.[12−18] Among the oxides, ZnO is one of the most studied for applications in LEDs, transistors, photovoltaics, catalysis, and sensing.[19−26] When highly doped with trivalent cations (usually Al^{3+} or Ga^{3+}), ZnO becomes a degenerate semiconductor as a result of the increased charge carrier (electron) concentration. Consequently, Al-doped ZnO (AZO), Ga-doped ZnO (GZO), and In-doped ZnO (IZO) all exhibit high electrical conductivity and surface plasmon resonance (SPR) peaks in the infrared spectrum, while also remaining transparent in the visible range.[27−29] This makes doped ZnO a valuable and cost-effective alternative to tin-doped indium oxide (ITO) for applications in transparent electrodes, electrochromics, and IR-absorbing coatings.[30,31]

To employ NCs successfully within such applications, synthetic methodologies that enable their large-scale production while maintaining high quality must first be developed. Of the various approaches currently available to grow doped NCs, hot-injection methods are the most commonly adopted to synthesize colloids of high quality and controlled properties;[32−35] however, these methods are unsuitable for production on an industrial level due to the inherent nonscalability of the hot-injection event.[36] Drawing from the broader NC field, where the use of non-injection (or heat-up) methods has become prevalent for large-scale reactions,[37−41] we present a facile method for the non-injection synthesis of high-quality ZnO NCs doped with trivalent cations. While ZnO NCs doped with substitutional divalent cations have been successfully synthesized at low temperatures and with large dopant concentration, the preparation of plasmonic ZnO colloids through the incorporation of trivalent ions with scalable methods still remains a major challenge.[42−45]

To achieve high-quality NCs using a non-injection approach, precise control of the nucleation and growth kinetics is critical.[37−40] This is achieved by understanding the reaction mechanism and controlling the side reactions.[41,46] Our system builds on seminal work by Peng and colleagues, who showed that under aliphatic conditions, esterification of zinc carboxylates with alcohols results in the formation of hydroxylated Zn species, which condense to nucleate ZnO NCs.[47] Here we expand on these previous investigations

* Address correspondence to enrico.dellagaspera@csiro.au, jacek.jasieniak@csiro.au.

Received for review May 20, 2014 and accepted August 6, 2014.

Published online August 19, 2014
10.1021/nn5027593

to demonstrate that small (15−20 nm), doped ZnO NCs can be grown under non-injection conditions with an unprecedented combination of high atomic doping levels (>15%), large reaction concentrations (0.2 M and greater), and high reaction yields (>90%).

RESULTS AND DISCUSSION

Doped ZnO NCs were synthesized by mixing zinc stearate ($ZnSt_2$), a metal (Al, Ga, In) acetylatetonate (AcAc) as dopant source, and oleic acid (OA) and 1-dodecanol (DDOL) as ligand and activating agent, respectively. The $ZnSt_2$ concentration in the solution was varied between 0.05 and 0.33 M using a noncoordinating solvent, 1-octadecene (ODE). The mixture was degassed briefly (3−5 min) at 25 °C and then heated to 100−140 °C under a nitrogen atmosphere to allow for the dissolution of all the solid precursors. The resulting clear solution was further heated to the target reaction temperature (200−250 °C) with a heating rate of ∼4 °C/min. After 3 h at the desired temperature, the solution was cooled naturally and the NCs were purified and dispersed in a suitable organic solvent, such as octane.

The reaction mechanism is presented in Scheme 1: it relies on the irreversible esterification between the carboxylate groups, which complex the metals and the hydroxyl moieties of DDOL. In this scheme, the metal precursors are represented as containing a combination of their initial ligands, namely stearate for Zn and AcAc for the dopant, as well as oleic acid (because partial substitution occurs during heating; see Supporting Information Figure S1). This ester elimination reaction has been widely studied for different combinations of metal carboxylates (stearates, acetates) and alcohols (benzyl alcohol, alkyl alcohols, alkyl diols).[45,47−51] It has been demonstrated that, by changing the relative amount of the acid, alcohol, and zinc sources, different morphologies of ZnO NCs can be obtained.[48,49] Moreover, free acids can cause partial dissolution of the NCs, liberating zinc carboxylate species that are eventually reincorporated into the NCs through a subsequent esterification, provided that the quantity of the alcohol is sufficient.[47] Tuning the relative amount of metal precursors, free ligand, and activating agent is therefore vital to obtain high-quality NCs under non-injection conditions.

These parameters are system specific, and in our study we observed the formation of large NCs with a large size distribution in reactions with low OA/DDOL ratios (generally <0.3). Conversely, if insufficient DDOL was used, the reaction yield was very low, even at high temperatures (up to 280 °C). To give rapid nucleation, small and isotropic NCs, high dopant levels, and near unity reaction yields, we found an optimum ratio between the ligand and the activating agent of ∼0.36 and a minimum alcohol/zinc ratio of ∼5 was required (optimization summarized in Table S1 and Figure S2).

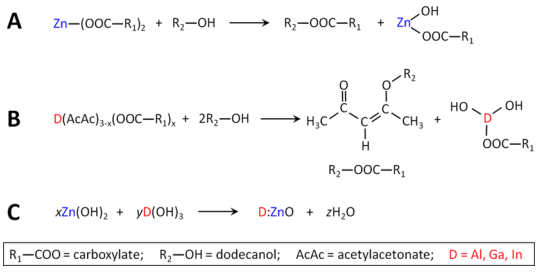

Scheme 1. Reaction between the zinc precursor (A) or the dopant precursor (B) and an alcohol leading to the formation of esters and hydroxylated metal species which eventually condense to form doped ZnO NCs (C).

Under these optimized reaction conditions, ZnO is readily doped with Al, Ga, and In. Figures 1 and 2 show the characterization of undoped and doped ZnO NCs, with those doped being prepared using a 20% molar ratio of dopant in solution with respect to Zn. A pronounced absorption in the near-infrared (NIR) is observed for all the colloidal solutions of doped NCs dispersed in tetrachloroethylene (TCE), while the solution of undoped ZnO remains transparent (Figure 1A). Notably, all samples are transparent in the visible spectrum. Due to a slightly larger NC size (see below), AZO colloidal solutions show a weak scattering tail within this spectral region. In comparison, doping NCs with In provides the best combination of high transparency in the visible and absorption in the IR range (see Figure S3).

The increased free electron density, stemming from extrinsic doping, is responsible for the rise of the SPR peak centered between 2.5 and 10 μm depending on the doping level.[27−29,52] Using FTIR spectroscopy, we studied the SPR feature of the AZO, GZO, and IZO NCs, identifying clearly broad plasmon peaks centered at about 7.5, 5, and 3 μm, respectively (Figure 1B and Figure S4). The SPR frequency of plasmonic NCs can be correlated with the density of charge carriers n according to the modified Drude−Lorentz theory using the following equation:[52−54]

$$n = \frac{\omega^2 m_e \varepsilon_0 (\varepsilon_\infty + 2\varepsilon_m)}{e^2}$$

where ω is the angular frequency corresponding to the SPR peak maximum, m_e is the effective mass of the electron, 0.24 times the free electron mass (9.11×10^{-31} kg), ε_0 is the permittivity of vacuum, 8.854×10^{-12} F m^{-1}, ε_∞ is the high-frequency dielectric constant (3.71 for ZnO), ε_m is the dielectric constant of the medium surrounding the NCs (2.27−2.5 for TCE), and e is the electron charge, 1.6×10^{-19} C.

Based on this formulism, free electron concentrations of $\sim 4.2 \times 10^{19}$, $\sim 9.4 \times 10^{19}$, and $\sim 2.6 \times 10^{20}$ cm^{-3} are estimated for AZO, GZO, and IZO, respectively. While this model provides only an approximation of the charge carrier density, since the position of the SPR peak is affected by a variety of parameters besides the density of charge carriers (NC size, shape, relative

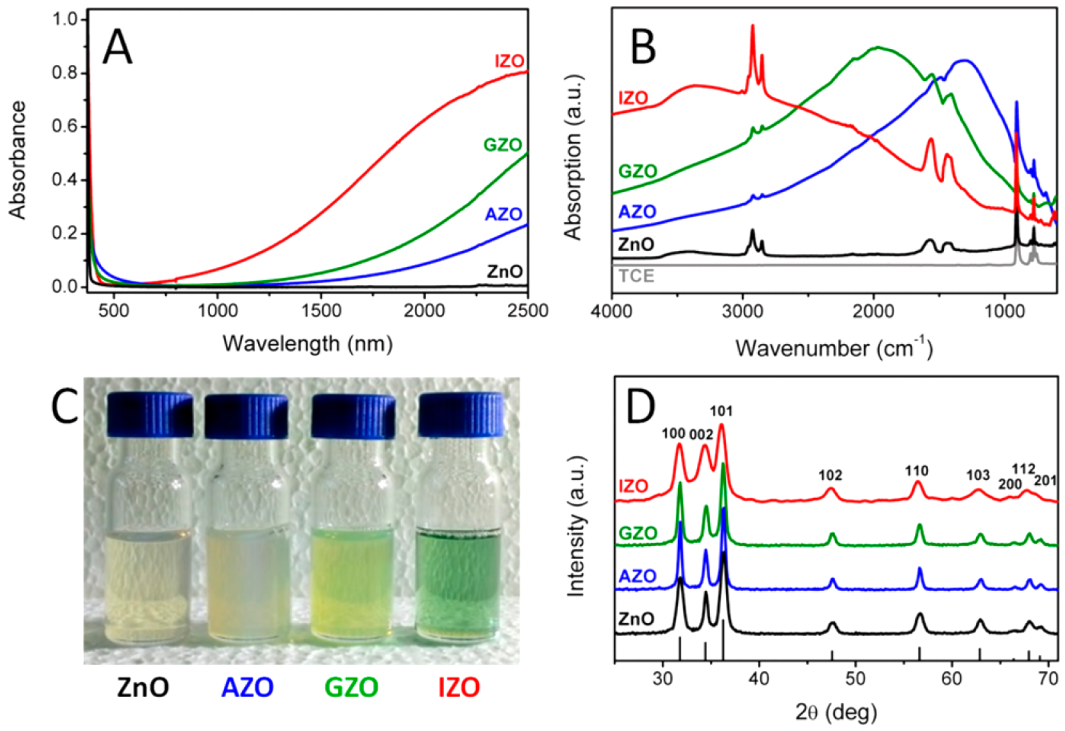

Figure 1. (A) Optical absorption spectra of equimolar solutions of ZnO-based NCs in TCE. (B) FTIR spectra of the same colloidal solutions. (C) Picture of the concentrated stock solutions (absorption spectra are obtained by diluting the stock solutions ~50 times). (D) XRD patterns of the dried powders (the predicted diffraction peaks for bulk wurtzite ZnO are displayed at the bottom).

proximity, defects, and segregation of dopants), it does provide a qualitative trend to the dopant-induced generation of free electrons within the ZnO NCs. Actual dopant incorporation within the ZnO NCs was evaluated using ICP. These measurements indeed confirmed a lower doping efficiency for aluminum (Al/Zn = 3.1%) with respect to gallium (Ga/Zn = 13.2%) and indium (In/Zn = 15.4%). This trend in doping efficiency (In > Ga > Al) is consistent with the gradually decreasing sizes of the trivalent dopants with respect to Zn^{2+}—the ionic radii for Zn^{2+}, Al^{3+}, Ga^{3+}, and In^{3+} in tetrahedral coordination as dictated by the ZnO wurtzite structure are 60, 39, 47, and 62 pm, respectively.[55] Greater similarity between the dopant and host cation size permits more favorable lattice substitution, ensuring that In^{3+} is most efficient at doping ZnO compared to the other cations. Additional evidence of the different doping levels comes from the prominent green-blue coloring of the solutions when ZnO is doped with In or Ga with respect to Al (Figure 1C). This is similar to the blue coloring observed in solutions of ITO NCs compared to yellowish In_2O_3 dispersions.[53,56]

To evaluate any possible effects of the dopants on the structure and morphology of ZnO, we used X-ray diffraction (XRD) and electron microscopy. All samples were found to possess the wurtzite ZnO phase (ICDD No. 36-1451) with no additional crystalline phases observed (Figure 1D). The crystallite sizes evaluated with the Scherrer relationship averaged over all the detected diffraction peaks were 12.3 ± 3.0, 20.8 ± 3.1, 16.0 ± 1.9, and 8.3 ± 2.3 nm for ZnO, AZO, GZO, and IZO, respectively (see Figure S5 for details). TEM (Figure 2 and Figure S6) and SEM (Figure 2) were additionally used to compare NC morphologies, showing that AZO NCs were larger and more faceted with predominantly pyramidal shapes, compared to the smaller and more spherical GZO and IZO colloids. Notably, undoped ZnO NCs showed both spherical and elongated shapes, similar to earlier observations.[27,47] The rod-like structures appear to be composed of a few NCs that have merged together, suggesting a preferential attachment of NCs to form elongated particles, as previously reported for ZnO and also other inorganic NCs.[57−59] Sizes based on TEM were in reasonable agreement with those determined by XRD, with the AZO, GZO, and IZO NCs being 27.1 ± 6.0, 17.5 ± 3.1, and 13.4 ± 2.4 nm, respectively. The average size of the isotropic undoped ZnO NCs was 11.2 ± 2.1 nm, while the merged ZnO NC rods possessed a diameter of 10.8 ± 1.9 nm and an average length of 21.6 ± 3.7 nm.

Despite these dopant-induced structural differences in the NCs, the reaction yields were fairly constant across the samples. By measuring the amount of dry powder collected after purification of the NCs and considering the presence of ~7 wt % of organic ligands as evidenced from thermogravimetric analysis (TGA, Figure S7), we estimated reaction yields to be consistently above 90%. This suggests that almost all precursors are consumed to give doped ZnO, regardless of the dopant.

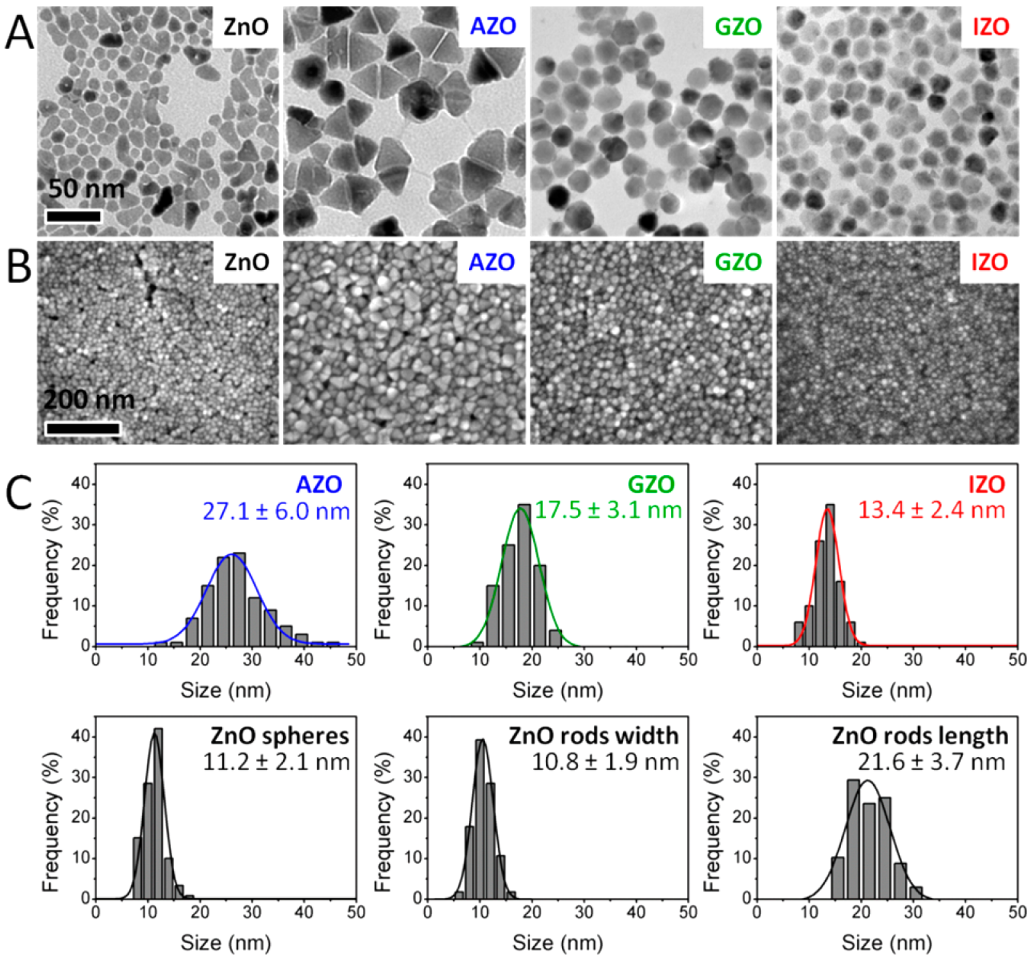

Figure 2. Electron microscopy characterization of ZnO-based NCs. (A) TEM images (the scale bar is the same in all TEM images). (B) SEM images (the scale bar is the same in all SEM images). (C) Histograms of size distribution evaluated from TEM images (see Figure S6 for additional TEM).

To further assess the effect of dopants in our system, we performed a control reaction by substituting the dopant precursors with $Zn(AcAc)_2$ at an analogous concentration. The results were almost identical compared to the those of the undoped ZnO synthesis, with only a minor increase in NC size observed, which can be simply ascribed to the larger total Zn content in solution. Importantly, no change in NC shape was observed, suggesting that the shape in the doped ZnO NCs is driven by the dopant cations (particularly Al) rather than the acetylacetonate chelating groups (Figure S8).

Besides the chemical nature of the dopant, several other parameters contribute to the evolution and final properties of the NCs, such as the amount of dopant precursor, the concentration of metal species in solution, as well as both the reaction duration and temperature. We investigated the influence of these parameters using GZO as a model system. GZO was chosen because of its strong IR absorption, while also avoiding the use of In, which makes it an attractive alternative to ITO. Figure 3A shows the effect of increasing the Ga/Zn ratio in the reaction medium on the optical properties of GZO NCs. A monotonic increase in IR absorption and a blue shift of the optical band gap are observed (Table S2). These are consistent with increasing dopant levels within the NCs, which results in the SPR peak being shifted to higher energies (Figure S9) and a more pronounced Burstein–Moss effect. For completeness, the latter is justified because the size of GZO NCs synthesized here are outside of the quantum confinement regime.[60,61]

ICP measurements showed that increasing the amount of $Ga(AcAc)_3$ up to a nominal Ga/Zn ratio of 30% caused a concordant increase in doping up to 15.8%. From a comparison of the nominal and actual Ga/Zn ratio (Figure 3B), we estimate a reactivity of the gallium precursor of about 70% at low doping levels, while at high doping levels the reactivity decreases to ~50%. This trend in doping levels was further confirmed by the charge carrier density estimated from the SPR peak position (Figure 3B and Figure S9) and also empirically from the progressive color change of GZO colloidal solutions and dried powders (Figure 3C). Notably, apart from a slight increase in crystallite size, no morphological differences in the NCs were

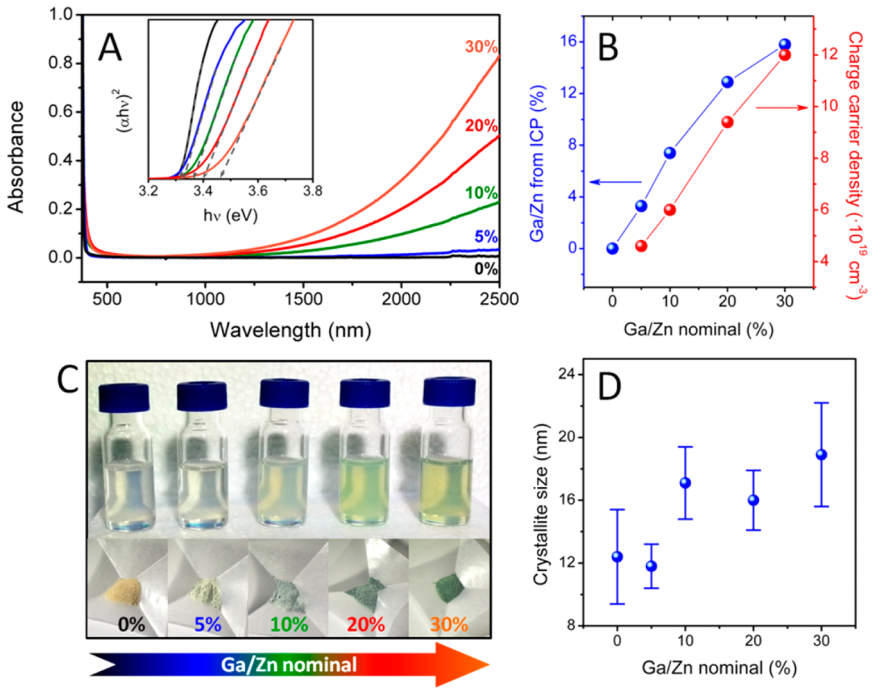

Figure 3. Effect of Ga concentration on the properties of GZO NCs. (A) Optical absorption spectra of equimolar solutions in TCE at different nominal Ga amounts (the inset shows the respective Tauc plots). (B) Ga/Zn ratios measured from ICP and respective charge carrier densities estimated from the SPR peak position as a function of the nominal amount of $Ga(AcAc)_3$ introduced. The lines act as guides for the eye. (C) Picture of the colloidal solutions and of the dry powders showing the color change as a function of doping. (D) Crystallite size as obtained from XRD analysis (full XRD patterns are reported in Figure S10).

observed within this doping range (Figure 3D and Figures S10 and S11). Interestingly, further increases to $Ga(AcAc)_3$ (Ga/Zn = 50%) resulted in no discernible increase to the IR absorption, despite ICP indicating that the amount of Ga exceeded 20% (Figure S12). While XRD showed no sign of Ga-rich crystalline phases, such as Ga_2O_3 or $ZnGa_2O_4$, we cannot exclude the presence of amorphous phases. Notably, an amorphous layer of niobium oxide surrounding Nb-doped TiO_2 NCs was recently reported to explain a similar observation.[62] This phenomenon is worth investigating further; however, it is outside the scope of the current study.

Having assessed how the amount of dopant precursor affects the final doping level, we now investigate the effect of reaction time on the evolution of doped ZnO NCs. Recent work on AZO NCs prepared through a hot-injection method showed that high doping levels required long reaction times (~5 h).[27] This result was attributed to slow NC growth and incremental dopant incorporation, which stems from the low reactivity of the vicinal diol chosen as the activating agent. In our system, a more reactive alcohol was used, DDOL, which increased the reaction kinetics and afforded doping within minutes of reaching the growth temperature (Figure 4A). Although the majority of the doping occurred within 15 min of reaction, the increase in the NIR absorption at longer times and the concomitant blue shift of the optical band gap (inset of Figure 4A and Table S2) provide direct evidence that the level of doping continued to slowly increase at longer times. Interestingly, we also observed a decrease in the absorption tail (extending from the UV absorption onset) over the course of the reaction (Figure 4A,B). We believe that this likely stems from a scattering contribution of sparingly soluble metal precursors that are gradually consumed and/or possible morphology effects (see Figure S13).[46,47]

Accompanying the above structural and optical changes during the reaction is the evolution of the chemical composition of the system. In Figure 4C,D, we show FTIR measurements made on the reaction medium as a function of time. Increasing the reaction duration induced a clear enhancement of the 1170, 1240, and 1730 cm^{-1} peaks, assigned to carbonyl groups in esters,[46−51] validating the proposed reaction mechanism depicted in Scheme 1. We also observed a concurrent decrease in the intensity of the peak centered at ~1710 cm^{-1}, due to OA, and of three peaks in the 1030−1080 cm^{-1} range, as well as the broad −OH band at 3000−3500 cm^{-1}, both of which are assigned to DDOL (Figure S14). The peaks at ~990 and ~1640 cm^{-1} (marked with a star) are due to ODE (Figure S14) and are used as a control to ensure that all the spectra are comparable. For completeness, control reactions performed without the metal precursors at the same temperature exhibited a similar evolution; however, the reaction medium containing metal carboxylates exhibited an enhanced rate of ester formation, consistent with esterification reactions being promoted by Lewis acids.[63]

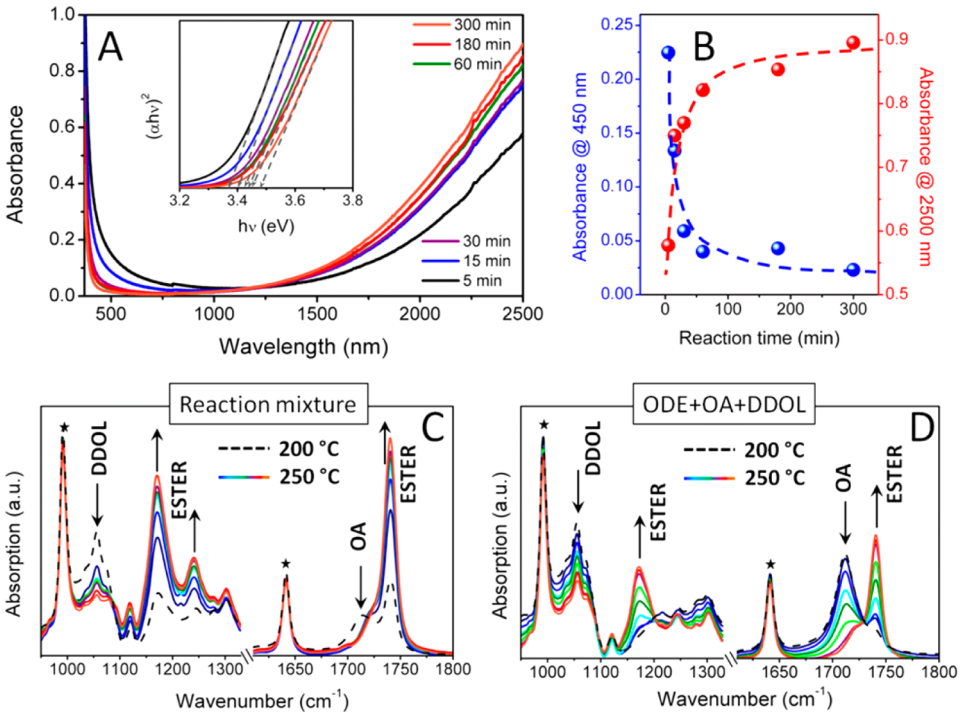

Figure 4. (A) Optical absorption spectra of GZO colloidal solutions at different reaction times (the inset shows the respective Tauc plot). (B) Evolution of absorbance in the visible (450 nm) and in the infrared (2500 nm) with reaction time. The lines act as guides for the eye. (C) FTIR spectra of the supernatant of the reaction solution at 200 °C (black dashed line) and at 250 °C at different times up to 300 min (blue to orange lines). (D) FTIR spectra of a mixture of ODE, OA, and DDOL heated at different times using the same conditions used to synthesize ZnO NCs. The stars mark the peaks assigned to ODE, while the arrows indicate the increase or decrease of significant peaks.

By analyzing the effects of dopant type and concentration, and of reaction duration, we have assessed the mechanism behind the nucleation of doped ZnO NCs and the strong influence of the synthetic conditions on the doping level. To further expand on this latter aspect, we now evaluate the remaining parameters, namely, zinc concentration and temperature. When synthesizing GZO NCs in dilute conditions ([$ZnSt_2$] = 0.05 M compared to syntheses presented up to this point which had [$ZnSt_2$] = 0.1 M) and keeping all the other parameters constant (Ga/Zn ratio, OA and DDOL amount), higher doping levels were recorded as presented in Figure 5A. Conversely, when $ZnSt_2$ was present at 0.33 M (no ODE added), lower Ga incorporation was observed. These findings suggest that under dilute conditions Ga exhibits a higher reactivity, enabling more facile incorporation within the ZnO lattice. The extent of doping also depends slightly on the final reaction temperature. We found that reactions carried out at 200 °C or above exhibited comparable doping levels, although slightly higher doping was achieved at 250 °C (Figure 5B). However, syntheses carried out below 190 °C produced little recoverable ZnO, suggesting a negligible reaction rate for both Zn and dopant precursors.

While the esterification of the alkyl carboxylates drives the formation of doped ZnO NCs, their ligation at the NC surface also renders the as-synthesized NCs soluble in organic solvents (Figure S3). As an example,

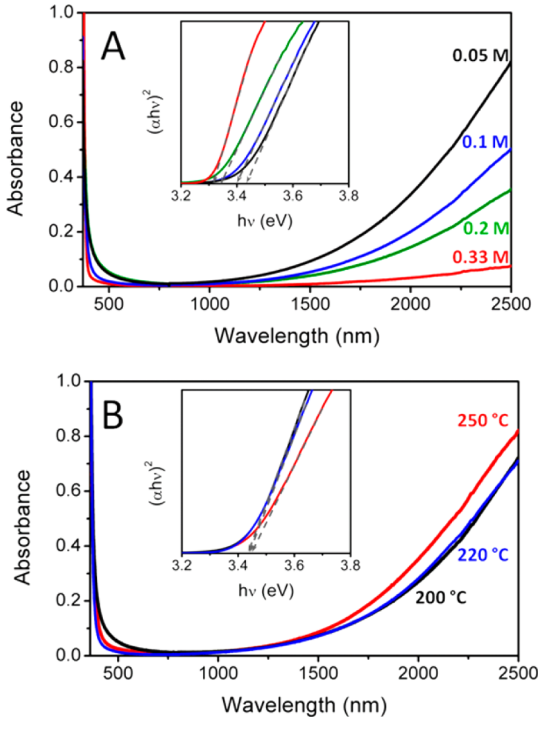

Figure 5. (A) Optical absorption spectra of GZO colloidal solutions in TCE synthesized at different zinc molarities using different amounts of ODE (the inset shows the respective Tauc plots). (B) Optical absorption spectra of GZO colloidal solutions in TCE synthesized at different temperatures (the inset shows the respective Tauc plots). The evaluated optical band gaps for all samples are listed in Table S2.

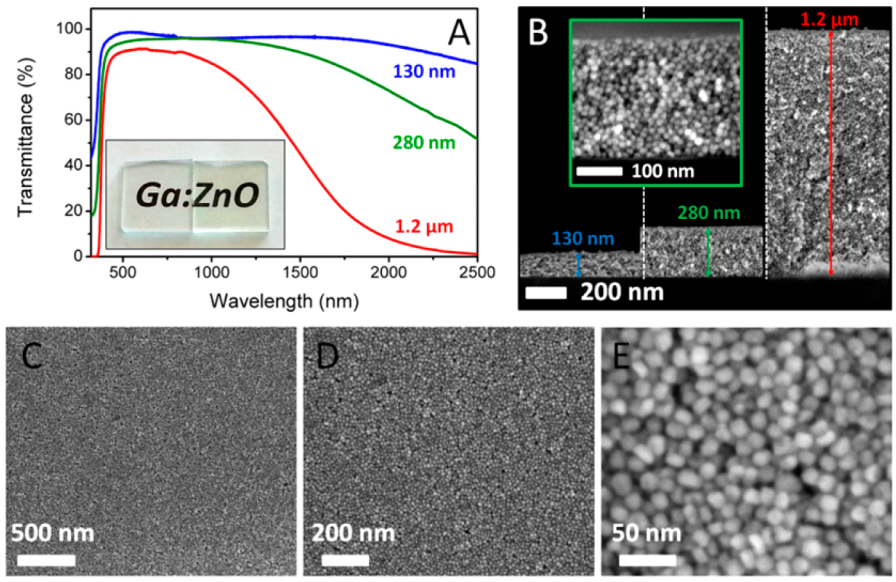

Figure 6. (A) Optical transmission spectra of GZO films with different thicknesses obtained from the same NC batch. The inset shows a picture of a glass slide (left) and of a glass slide coated with a GZO film (right). (B) SEM images in cross section showing the actual thickness of the three samples. The inset shows an enlarged view of the 280 nm thick sample. (C–E) SEM images in top view at different magnifications showing the uniformity of the deposited films.

stable dispersions in octane at concentrations up to 100 mg mL^{-1} were readily prepared. These were used to deposit high-quality GZO films *via* spin-coating or drop-casting on different substrates (glass, silicon). The layers were homogeneous, highly transparent in the visible (transmittance >90%) and absorbing in the NIR according to the doping level and/or thickness (Figure 6). While unlocking the true potential of such films for optoelectronic properties will require some degree of surface engineering, this example of an IR absorbing and visibly transparent coating clearly demonstrates that our GZO NCs are ideal starting materials for a variety of thin-film applications.

CONCLUSION

In conclusion, we have presented a detailed study into the non-injection synthesis of ZnO-based plasmonic nanocrystals. Through the controlled doping of trivalent Al, Ga, and In ions within the ZnO lattice, such nanocrystals exhibit a surface plasmon resonance in the infrared that is directly correlated to the doping level. Importantly, this tunability in the optical properties is achieved using a simple synthetic method that is reproducible, yields nearly monodisperse ZnO-based colloids, can be performed at high concentrations with near unity reaction yields, and can readily achieve atomic doping levels over 15%. Collectively, these advances represent a step forward to harnessing the true potential of solution-processing for the development of next-generation optoelectronic devices, in particular, those requiring high visible transparency and controllable infrared absorption.

METHODS

Materials. All chemicals have been used without further purification. Zinc stearate ($ZnSt_2$, technical) was supplied by BDH-Prolabo. Gallium(III) acetylacetonate ($Ga(AcAc)_3$, 99.99%), indium(III) acetylacetonate ($In(AcAc)_3$, 99.99%), oleic acid (OA, 90%), 1-dodecanol (DDOL, 99%), and 1-octadecene (ODE, 90%) were supplied by Sigma-Aldrich. Aluminum(III) acetylacetonate ($Al(AcAc)_3$, 99%) was supplied by Strem Chemicals. Chloroform (99.8%), tetrachloroethylene (TCE, 99%), toluene (99.9%), acetone (99.8%), methanol (99.8%), and ethanol (99.9%) were purchased from Merck. Octane (98%) was supplied by Alfa Aesar.

Nanocrystal Synthesis. After an initial optimization of the ligand (OA) and activating agent (DDOL) amounts with respect to $ZnSt_2$ (see Table S1 and Figure S2), the different reactions have been carried out by fixing the $ZnSt_2$/DDOL/OA ratios and changing other parameters (dopant type and amount, temperature, time, Zn concentration).

In a typical synthesis (results presented in Figures 1 and 2), 1.89 g of $ZnSt_2$ was mixed with 4.8 g of DDOL, 2.65 g of OA, and 195 mg of $Al(AcAc)_3$ (or 220 mg $Ga(AcAc)_3$ or 247 mg $In(AcAc)_3$, resulting in a nominal doping level of 20% with respect to $ZnSt_2$) in a round-bottom flask. ODE was then added (21 mL to produce a final concentration of 0.1 M), and the flask was connected to a Schlenk line and degassed at room temperature for 3–5 min. The flask was then purged with nitrogen and kept under a nitrogen atmosphere for the duration of the whole reaction. The temperature was increased to 100–140 °C, and the solution was kept at this temperature for at least 20 min to ensure complete dissolution and homogenization of the different reagents (no appreciable differences were observed in the final product if this step was varied between 100 and 140 °C). The solution was then heated to 250 °C under strong stirring at a slow heating rate of ~4 °C/min. Three hours after reaching the target temperature, the flask was removed from the heating source and allowed to cool to room temperature naturally.

To analyze the effect of the reaction conditions, different $Ga(AcAc)_3$ amounts (55, 110, 220, 330, and 550 mg to give nominal doping levels of 5, 10, 20, 30, and 50%, respectively, Figure 3 and Figures S9–S12) or different amounts of ODE (51, 21, 6 mL, and none for 0.05, 0.1, 0.2, and 0.33 M, respectively,

Figure 5A) were used. Moreover, different reaction times (up to 5 h, Figure 4 and Figures S13 and S14) and different reaction temperatures (in the 200−250 °C range, Figure 5B) were also investigated.

The final solution was then diluted with toluene, and the NCs were flocculated using acetone. After centrifugation (4000 rpm, 4 min), the NCs were easily redispersed in organic solvents such as chloroform, TCE, hexane, or octane. Further cycles of common precipitation/redispersion procedures using toluene/acetone, TCE/acetone, or chloroform/ethanol as solvent/nonsolvent couples could be carried out to purify the colloids and remove the unreacted reagents.

Thin films were prepared by spin-coating a concentrated solution (50−100 mg mL^{-1}) in octane at 1000 rpm for 30 s and dried on a hot plate at 100 °C for 5 min. Alternatively, samples were drop-cast from a diluted solution (10−20 mg mL^{-1}) of NCs in either chloroform or hexane at room temperature, and once the solvent evaporated, the films were stabilized on a hot plate at 100 °C for 5 min.

Characterization Techniques. Optical absorption spectra of colloidal solutions in TCE and of thin films on glass substrates were measured using a Varian-Cary 5E spectrophotometer in the 300−2500 nm range. X-ray diffraction patterns of the prepared powders were collected using a Bruker D8 diffractometer equipped with a Cu Kα radiation source and operated at 40 mV and 40 mA. The crystallite size was evaluated with the Scherrer relationship using the full width at half-maximum obtained by fitting the main nine diffraction peaks detected between 30 and 75° with Lorentzian functions. The resulting crystallite sizes are provided as the average between the values obtained from the nine different peaks, using one standard deviation as error on the measurements.

The chemical composition of the prepared powders was analyzed by inductively coupled plasma optical emission spectroscopy (ICP-OES using an Agilent 700 Series instrument) and inductively coupled plasma mass spectrometry (ICP-MS using an Agilent 7700 instrument): dry powders were digested in nitric acid at 105 °C, and after digestion, they were diluted appropriately and analyzed for Zn amount by ICP-OES and for dopant amount by ICP-MS.

Transmission electron microscopy (TEM) images of colloids deposited on carbon-coated copper grids were taken using a Fei Tecnai 12 G2 microscope operating at 120 kV equipped with an Olympus MegaView III CCD camera.

Samples of NCs deposited on silicon substrates were imaged using a Fei Helios Nanolab 600 scanning electron microscope (SEM). Fourier transform infrared spectroscopy (FTIR) data were collected on a Thermo Scientific Nicolet 6700 spectrometer on a laminated diamond mounted in a stainless steel plate in the 4000−600 cm^{-1} range with a resolution of 4 cm^{-1}. IR spectra of solvents and reaction solutions were measured as liquids, while ZnO-based NCs were-drop cast from TCE to form a thin film upon evaporation of the solvent.

Thermogravimetric analysis measurements of dried powders were performed on a Mettler Toledo TGA/SDTA851e instrument in the temperature range of 30−800 °C at 10 °C/min with a gas (dry air or nitrogen) flow of 30 mL min^{-1}.

Conflict of Interest: The authors declare no competing financial interest.

Acknowledgment. This work was funded through the Flexible Electronics Theme of the Future Manufacturing Flagship as part of an Office of the Chief Executive Postdoctoral Fellowship to E.D.G. The Australian Research Council is acknowledged for funding through the Grant DP110105341 and a DECRA, by J.J.J. and A.S.R.C., respectively.

Supporting Information Available: Additional characterizations and data: UV−vis−NIR absorption spectra, FTIR, XRD, SEM, TEM, TGA (Figures S1−S14 and Tables S1 and S2). This material is available free of charge *via* the Internet at http://pubs.acs.org.

REFERENCES AND NOTES

1. Norris, D. J.; Efros, A. L.; Erwin, S. C. Doped Nanocrystals. *Science* **2008**, *319*, 1776–1779.
2. Zhao, Y.; Pan, H.; Lou, Y.; Qiu, X.; Zhu, J.; Burda, C. Plasmonic $Cu_{2-x}S$ Nanocrystals: Optical and Structural Properties of Copper-Deficient Copper(I) Sulfides. *J. Am. Chem. Soc.* **2009**, *131*, 4253–4261.
3. Luther, M. J.; Jain, P. K.; Ewers, T.; Alivisatos, A. P. Localized Surface Plasmon Resonances Arising from Free Carriers in Doped Quantum Dots. *Nat. Mater.* **2011**, *10*, 361–366.
4. Hsu, S.-W.; On, K.; Tao, A. R. Localized Surface Plasmon Resonances of Anisotropic Semiconductor Nanocrystals. *J. Am. Chem. Soc.* **2011**, *133*, 19072–19075.
5. Dorfs, D.; Härtling, T.; Miszta, K.; Bigall, N. C.; Kim, M. R.; Genovese, A.; Falqui, A.; Povia, M.; Manna, L. Reversible Tunability of the Near-Infrared Valence Band Plasmon Resonance in $Cu_{2-x}Se$ Nanocrystals. *J. Am. Chem. Soc.* **2011**, *133*, 11175–11180.
6. Niezgoda, J. S.; Harrison, M. A.; McBride, J. R.; Rosenthal, S. J. Novel Synthesis of Chalcopyrite $Cu_xIn_yS_2$ Quantum Dots with Tunable Localized Surface Plasmon Resonances. *Chem. Mater.* **2012**, *24*, 3294–3298.
7. Palomaki, P. K. B.; Miller, E. M.; Neale, N. R. Control of Plasmonic and Interband Transitions in Colloidal Indium Nitride Nanocrystals. *J. Am. Chem. Soc.* **2013**, *135*, 14142–14150.
8. Manna, G.; Bose, R.; Pradhan, N. Semiconducting and Plasmonic Copper Phosphide Platelets. *Angew. Chem., Int. Ed.* **2013**, *52*, 6762–6766.
9. Liu, X.; Wang, X.; Zhou, B.; Law, W.-C.; Cartwright, A. N.; Swihart, M. T. Size-Controlled Synthesis of $Cu_{2-x}E$ (E = S, Se) Nanocrystals with Strong Tunable Near-Infrared Localized Surface Plasmon Resonance and High Conductivity in Thin Films. *Adv. Funct. Mater.* **2013**, *23*, 1256–1264.
10. Polking, M. J.; Jain, P. K.; Bekenstein, Y.; Banin, U.; Millo, O.; Ramesh, R.; Alivisatos, A. P. Controlling Localized Surface Plasmon Resonances in GeTe Nanoparticles Using an Amorphous-to-Crystalline Phase Transition. *Phys. Rev. Lett.* **2013**, *111*, 037401.
11. Faucheaux, J. A.; Stanton, A. L. D.; Jain, P. K. Plasmon Resonances of Semiconductor Nanocrystals: Physical Principles and New Opportunities. *J. Phys. Chem. Lett.* **2014**, *5*, 976–985.
12. Kanehara, M.; Koike, H.; Yoshinaga, T.; Teranishi, T. Indium Tin Oxide Nanoparticles with Compositionally Tunable Surface Plasmon Resonance Frequencies in the Near-IR Region. *J. Am. Chem. Soc.* **2009**, *131*, 17736–17737.
13. Manthiram, K.; Alivisatos, A. P. Tunable Localized Surface Plasmon Resonances in Tungsten Oxide Nanocrystals. *J. Am. Chem. Soc.* **2012**, *134*, 3995–3998.
14. Gordon, T. R.; Cargnello, M.; Paik, T.; Mangolini, F.; Weber, R. T.; Fornasiero, P.; Murray, C. B. Nonaqueous Synthesis of TiO_2 Nanocrystals Using TiF_4 To Engineer Morphology, Oxygen Vacancy Concentration, and Photocatalytic Activity. *J. Am. Chem. Soc.* **2012**, *134*, 6751–6761.
15. Gordon, T. R.; Paik, T.; Klein, D. R.; Naik, G. V.; Caglayan, H.; Boltasseva, A.; Murray, C. B. Shape-Dependent Plasmonic Response and Directed Self-Assembly in a New Semiconductor Building Block, Indium-Doped Cadmium Oxide (ICO). *Nano Lett.* **2013**, *13*, 2857–2863.
16. Schimpf, A. M.; Thakkar, N.; Gunthardt, C. E.; Masiello, D. J.; Gamelin, D. R. Charge-Tunable Quantum Plasmons in Colloidal Semiconductor Nanocrystals. *ACS Nano* **2014**, *8*, 1065–1072.
17. Mattox, T. M.; Bergerud, A.; Agrawal, A.; Milliron, D. J. Nb-Doped Colloidal TiO_2 Nanocrystals with Tunable Infrared Absorption. *Chem. Mater.* **2014**, *26*, 1779–1784.
18. Lounis, S. D.; Runnerstrom, E. L.; Llordes, A.; Milliron, D. J. Defect Chemistry and Plasmon Physics of Colloidal Metal Oxide Nanocrystals. *J. Phys. Chem. Lett.* **2014**, *5*, 1564–1574.
19. Yang, J. L.; An, S. J.; Park, W. I.; Yi, G.-C.; Choi, W. Photocatalysis Using ZnO Thin Films and Nanoneedles Grown by Metal−Organic Chemical Vapor Deposition. *Adv. Mater.* **2004**, *16*, 1661–1664.
20. Wang, X.; Summers, C. J.; Wang, Z. L. Large-Scale Hexagonal-Patterned Growth of Aligned ZnO Nanorods for Nano-optoelectronics and Nanosensor Arrays. *Nano Lett.* **2004**, *4*, 423–426.

21. Park, W. I.; Kim, J. S.; Yi, G.-C.; Bae, M. H.; Lee, H.-J. Fabrication and Electrical Characteristics of High-Performance ZnO Nanorod Field-Effect Transistors. *Appl. Phys. Lett.* **2004**, *85*, 5052–5054.
22. Tsukazaki, A.; Ohtomo, A.; Onuma, T.; Ohtani, M.; Makino, T.; Sumiya, M.; Ohtani, K.; Chichibu, S. F.; Fuke, S.; Segawa, Y.; *et al.* Repeated Temperature Modulation Epitaxy for p-Type Doping and Light-Emitting Diode Based on ZnO. *Nat. Mater.* **2005**, *4*, 42–46.
23. Wang, H. T.; Kang, B. S.; Ren, F.; Tien, L. C.; Sadik, P. W.; Norton, D. P.; Pearton, S. J.; Lin, J. Hydrogen-Selective Sensing at Room Temperature with ZnO Nanorods. *Appl. Phys. Lett.* **2005**, *86*, 243503.
24. Morfa, A. J.; Beane, G.; Mashford, B.; Singh, B.; Della Gaspera, E.; Martucci, A.; Mulvaney, P. Fabrication of ZnO Thin Films from Nanocrystal Inks. *J. Phys. Chem. C* **2010**, *114*, 19815–19821.
25. Sun, Y.; Seo, J. H.; Takacs, C. J.; Seifter, J.; Heeger, A. J. Inverted Polymer Solar Cells Integrated with a Low-Temperature-Annealed Sol–Gel-Derived ZnO Film as an Electron Transport Layer. *Adv. Mater.* **2011**, *23*, 1679–1683.
26. Della Gaspera, E.; Guglielmi, M.; Perotto, G.; Agnoli, S.; Granozzi, G.; Post, M. L.; Martucci, A. CO Optical Sensing Properties of Nanocrystalline ZnO–Au Films: Effect of Doping with Transition Metal Ions. *Sens. Actuators, B* **2012**, *161*, 675–683.
27. Buonsanti, R.; Llordes, A.; Aloni, S.; Helms, B. A.; Milliron, D. J. Tunable Infrared Absorption and Visible Transparency of Colloidal Aluminum-Doped Zinc Oxide Nanocrystals. *Nano Lett.* **2011**, *11*, 4706–4710.
28. Della Gaspera, E.; Bersani, M.; Cittadini, M.; Guglielmi, M.; Pagani, D.; Noriega, R.; Mehra, S.; Salleo, A.; Martucci, A. Low-Temperature Processed Ga-Doped ZnO Coatings from Colloidal Inks. *J. Am. Chem. Soc.* **2013**, *135*, 3439–3448.
29. Cimitan, S.; Albonetti, S.; Forni, L.; Peri, F.; Lazzari, D. Solvothermal Synthesis and Properties Control of Doped ZnO Nanoparticles. *J. Colloid Interface Sci.* **2009**, *329*, 73–80.
30. Chung, C.-H.; Song, T.-B.; Bob, B.; Zhu, R.; Duan, H.-S.; Yang, Y. Silver Nanowire Composite Window Layers for Fully Solution-Deposited Thin-Film Photovoltaic Devices. *Adv. Mater.* **2012**, *24*, 5499–5504.
31. Llordes, A.; Garcia, G.; Gazquez, J.; Milliron, D. J. Tunable Near-Infrared and Visible Light Transmittance in Nanocrystal-in-Glass Composites. *Nature* **2013**, *500*, 323–326.
32. Stowell, C. A.; Wiacek, R. J.; Saunders, A. E.; Korgel, B. A. Synthesis and Characterization of Dilute Magnetic Semiconductor Manganese-Doped Indium Arsenide Nanocrystals. *Nano Lett.* **2003**, *3*, 1441–1447.
33. Thakar, R.; Chen, Y.; Snee, P. T. Efficient Emission from Core/(Doped) Shell Nanoparticles: Applications for Chemical Sensing. *Nano Lett.* **2007**, *7*, 3429–3432.
34. Chen, D.; Viswanatha, R.; Ong, G. L.; Xie, R.; Balasubramaninan, M.; Peng, X. Temperature Dependence of "Elementary Processes" in Doping Semiconductor Nanocrystals. *J. Am. Chem. Soc.* **2009**, *131*, 9333–9339.
35. Brovelli, S.; Galland, C.; Viswanatha, R.; Klimov, V. I. Tuning Radiative Recombination in Cu-Doped Nanocrystals *via* Electrochemical Control of Surface Trapping. *Nano Lett.* **2012**, *12*, 4372–4379.
36. Cao, Y. C.; Wang, J. One-Pot Synthesis of High-Quality Zinc-Blende CdS Nanocrystals. *J. Am. Chem. Soc.* **2004**, *126*, 14336–14337.
37. Park, J.; An, K.; Hwang, Y.; Park, J.-G.; Noh, H.-J.; Kim, J.-Y.; Park, J.-H.; Hwang, N.-M.; Hyeon, T. Ultra-Large-Scale Syntheses of Monodisperse Nanocrystals. *Nat. Mater.* **2004**, *3*, 891–895.
38. Yang, Y. A.; Wu, H.; Williams, K. R.; Cao, Y. C. Synthesis of CdSe and CdTe Nanocrystals without Precursor Injection. *Angew. Chem., Int. Ed.* **2005**, *44*, 6712–6715.
39. Liu, Q.; Yan, Z.; Henderson, N. L.; Bauer, J. C.; Goodman, D. W.; Batteas, J. D.; Schaak, R. E. Synthesis of CuPt Nanorod Catalysts with Tunable Lengths. *J. Am. Chem. Soc.* **2009**, *131*, 5720–5721.
40. Timonen, J. V. I.; Seppala, E. T.; Ikkala, O.; Ras, R. H. A. From Hot-Injection Synthesis to Heating-Up Synthesis of Cobalt Nanoparticles: Observation of Kinetically Controllable Nucleation. *Angew. Chem., Int. Ed.* **2011**, *50*, 2080–2084.
41. Chesman, A. S. R.; van Embden, J.; Duffy, N. W.; Webster, N. A. S.; Jasieniak, J. J. *In Situ* Formation of Reactive Sulfide Precursors in the One-Pot, Multigram Synthesis of Cu_2ZnSnS_4 Nanocrystals. *Cryst. Growth Des.* **2013**, *13*, 1712–1720.
42. Schwartz, D. A.; Norberg, N. S.; Nguyen, Q. P.; Parker, J. M.; Gamelin, D. R. Magnetic Quantum Dots: Synthesis, Spectroscopy, and Magnetism of Co^{2+}- and Ni^{2+}-Doped ZnO Nanocrystals. *J. Am. Chem. Soc.* **2003**, *125*, 13205–13218.
43. Norberg, N. S.; Kittilstved, K. R.; Amonette, J. E.; Kukkadapu, R. K.; Schwartz, D. A.; Gamelin, D. R. Synthesis of Colloidal Mn^{2+}:ZnO Quantum Dots and High-TC Ferromagnetic Nanocrystalline Thin Films. *J. Am. Chem. Soc.* **2004**, *126*, 9387–9398.
44. Wang, Y. S.; Thomas, P. J.; O'Brien, P. Optical Properties of ZnO Nanocrystals Doped with Cd, Mg, Mn, and Fe Ions. *J. Phys. Chem. B* **2006**, *110*, 21412–21415.
45. Yang, Y.; Jin, Y.; He, H.; Wang, Q.; Tu, Y.; Lu, H.; Ye, Z. Dopant-Induced Shape Evolution of Colloidal Nanocrystals: The Case of Zinc Oxide. *J. Am. Chem. Soc.* **2010**, *132*, 13381–13394.
46. Chen, Y.; Johnson, E.; Peng, X. Formation of Monodisperse and Shape-Controlled MnO Nanocrystals in Non-injection Synthesis: Self-Focusing *via* Ripening. *J. Am. Chem. Soc.* **2007**, *129*, 10937–10947.
47. Chen, Y.; Kim, M.; Lian, G.; Johnson, M. B.; Peng, X. Side Reactions in Controlling the Quality, Yield, and Stability of High Quality Colloidal Nanocrystals. *J. Am. Chem. Soc.* **2005**, *127*, 13331–13337.
48. Joo, J.; Kwon, S. G.; Yu, J. H.; Hyeon, T. Synthesis of ZnO Nanocrystals with Cone, Hexagonal Cone, and Rod Shapes *via* Non-hydrolytic Ester Elimination Sol–Gel Reactions. *Adv. Mater.* **2005**, *17*, 1873–1877.
49. Clavel, G.; Willinger, M.-G.; Zitoun, D.; Pinna, N. Solvent Dependent Shape and Magnetic Properties of Doped ZnO Nanostructures. *Adv. Funct. Mater.* **2007**, *17*, 3159–3169.
50. Zhong, X.; Feng, Y.; Zhang, Y.; Lieberwirth, I.; Knoll, W. Nonhydrolytic Alcoholysis Route to Morphology-Controlled ZnO Nanocrystals. *Small* **2007**, *3*, 1194–1199.
51. Bilecka, I.; Elser, P.; Niederberger, M. Kinetic and Thermodynamic Aspects in the Microwave-Assisted Synthesis of ZnO Nanoparticles in Benzyl Alcohol. *ACS Nano* **2009**, *3*, 467–477.
52. Faucheaux, J. A.; Jain, P. K. Plasmons in Photocharged ZnO Nanocrystals Revealing the Nature of Charge Dynamics. *J. Phys. Chem. Lett.* **2013**, *4*, 3024–3030.
53. Wang, T.; Radovanovic, P. V. Free Electron Concentration in Colloidal Indium Tin Oxide Nanocrystals Determined by Their Size and Structure. *J. Phys. Chem. C* **2011**, *115*, 406–413.
54. Link, S.; El-Sayed, M. A. Spectral Properties and Relaxation Dynamics of Surface Plasmon Electronic Oscillations in Gold and Silver Nanodots and Nanorods. *J. Phys. Chem. B* **1999**, *103*, 8410–8426.
55. Shannon, R. D. Revised Effective Ionic Radii and Systematic Studies of Interatomic Distances in Halides and Chalcogenides. *Acta Crystallogr.* **1974**, *A32*, 751–767.
56. Lee, J.; Lee, S.; Li, G.; Petruska, M. A.; Paine, D. C.; Sun, S. A Facile Solution-Phase Approach to Transparent and Conducting ITO Nanocrystal Assemblies. *J. Am. Chem. Soc.* **2012**, *134*, 13410–13414.
57. Tang, Z.; Kotov, N. A.; Giersig, M. Spontaneous Organization of Single CdTe Nanoparticles into Luminescent Nanowires. *Science* **2002**, *297*, 237–240.
58. Pacholski, C.; Kornowski, A.; Weller, H. Self-Assembly of ZnO: From Nanodots to Nanorods. *Angew. Chem., Int. Ed.* **2002**, *41*, 1188–1191.
59. Cho, K.-S.; Talapin, D. V.; Gaschler, W.; Murray, C. B. Designing PbSe Nanowires and Nanorings through Oriented Attachment of Nanoparticles. *J. Am. Chem. Soc.* **2005**, *127*, 7140–7147.

60. Redmond, G.; O'Keeffe, A.; Burgess, C.; MacHale, C.; Fitzmaurice, D. Spectroscopic Determination of the Flatband Potential of Transparent Nanocrystalline ZnO Films. *J. Phys. Chem.* **1993**, *97*, 11081–11086.
61. Wood, A.; Giersig, M.; Hilgendorff, M.; Vilas-Campos, A.; Liz-Marzan, L. M.; Mulvaney, P. Size Effects in ZnO: The Cluster to Quantum Dot Transition. *Aust. J. Chem.* **2003**, *56*, 1051–1057.
62. De Trizio, L.; Buonsanti, R.; Schimpf, A. M.; Llordes, A.; Gamelin, D. R.; Simonutti, R.; Milliron, D. J. Nb-Doped Colloidal TiO_2 Nanocrystals with Tunable Infrared Absorption. *Chem. Mater.* **2013**, *25*, 3383–3390.
63. Di Serio, M.; Tesser, R.; Dimiccoli, M.; Cammarota, F.; Nastasi, M.; Santacesaria, E. Synthesis of Biodiesel *via* Homogeneous Lewis Acid Catalyst. *J. Mol. Catal. A: Chem.* **2005**, *239*, 111–115.